

Testing MSW effect in Supernova Explosion with Neutrino event rates

Kwang-Chang Lai,¹ C. S. Jason Leung,² and Guey-Lin Lin²

¹*Center for General Education, Chang Gung University, Kwei-Shan, Taoyuan, 333, Taiwan*

²*Institute of Physics, National Chiao Tung University, Hsinchu, 300, Taiwan*

Flavor transitions in supernova neutrinos are yet to be determined. We present a method to probe whether or not the Mikheyev-Smirnov-Wolfenstein effects occur as SN neutrinos propagate outward from the SN core by investigating time evolutions of neutrino event rates for different flavors in different kinds of detectors. As the MSW effect occurs, the ν_e flux swaps with the ν_x flux, which represents any one of ν_μ , ν_τ , $\bar{\nu}_\mu$, and $\bar{\nu}_\tau$ flux, either fully or partially depending on the neutrino mass hierarchy. During the neutronization burst, the ν_e emission evolves in a much different shape from the emissions of $\bar{\nu}_e$ and ν_x while the latter two evolve in a similar pattern. Meanwhile, the luminosity of the ν_e emission is much larger than those of the $\bar{\nu}_e$ and ν_x emissions while the latter two are roughly equal. As a consequence, the time-evolution pattern of the ν_e Ar event rates in the absence of the MSW effect will be much different from that in the occurrence of the MSW effect, in either mass hierarchy. With the simulated SN neutrino emissions, the ν_e Ar and inverse beta decay event rates are evaluated. The ratios of the two cumulative event rates are calculated for different progenitor masses up to 100 ms. We show that the time evolutions of this cumulative ratios can effectively determine whether MSW effects really occur for SN neutrinos or not.

PACS numbers: 95.85.Ry, 14.60.Pq, 95.55.Vj

I. INTRODUCTION

Flavor transitions of SN neutrinos have been an attractive field of research and motivated numerous efforts (See [1] for a review) on flavor changing during the gravitational core collapse of a massive star. Originating from deep inside the SN core, neutrinos are expected to experience significant flavor transitions as they propagate outward to the ter-

restrial detectors. On account of MSW effects ν_e and $\bar{\nu}_e$ fluxes will swap with ν_x flux fully or partially when the neutrino vacuum oscillation frequency $\omega = \Delta m^2/2E$ is of the order of the matter potential, $\lambda = \sqrt{2}G_F n_e$. Here Δm^2 denotes one of the mass-squared differences, E the neutrino energy, and n_e the net electron density. For typical SN post-bounce matter profiles, this MSW-induced flavor conversions occur at distances of $\sim \mathcal{O}(10^3)$ km from the SN core where $\omega \simeq \lambda$ [2].

In the deep region of the core where the neutrino densities are large, the off-diagonal $\nu - \nu$ potential, $\mu \sim \sqrt{2}G_F n_\nu$, arising from coherent $\nu - \nu$ forward scatterings, may induce collective pair flavor oscillation $\nu_e \bar{\nu}_e \leftrightarrow \nu_x \bar{\nu}_x$ with a frequency $\sim \sqrt{\omega\mu}$ over the entire energy range. Based on theoretical understanding and numerical calculations, large collective flavor conversions were predicted to occur at distances of $\sim \mathcal{O}(10^2)$ km from the SN core where $\omega \simeq \mu$ [3–5].

Very close ($\sim \mathcal{O}(1)$ m) to the SN surface, the $\nu - \nu$ potential may induce even faster flavor conversions at a rate $\sim \mu$ than the above collective oscillation at a rate $\sim \sqrt{\omega\mu}$ [6]. This fast flavor conversion requires sufficiently different angular distributions for different neutrino flavors [7–9]. Since the flavor ν_x decouples from matter earlier than $\bar{\nu}_e$, and the latter decouples earlier than ν_e , it can be expected that the radius of ν_e sphere, r_{ν_e} , is larger than that of $\bar{\nu}_e$ sphere, $r_{\bar{\nu}_e}$, which in turn should be larger than r_{ν_x} . Therefore, close to the SN surface, r_{ν_e} , the ν_x zenith-angle distribution would be more forward-peaked than that of $\bar{\nu}_e$, which in turn would be more forward-peaked than the ν_e distribution.

Flavor transitions are expected to change flavor compositions of primary SN neutrino fluxes and, hence, to leave imprints in neutrino events measured in terrestrial detectors. This motivates our study of probing flavor transitions with measurements of galactic SN neutrinos arriving at the Earth. Unlike the status of MSW effects, consensus on collective flavor transitions has not yet been reached so that studies of collective flavor transition effects on terrestrial SN neutrino fluxes are few. Meanwhile, the study of fast flavor conversions has just started in recent years and is still far from a thorough understanding. Therefore, we focus on MSW effects in SN neutrinos. Based on the understanding that MSW effects are sensitive to neutrino mass hierarchy (NMH), lots of studies [10–16] are devoted to probing NMH with SN neutrino events detected on the Earth. Naturally, these studies all assume the occurrence of MSW effects. In this paper, we however would like to determine whether MSW effects really occur in SN neutrinos or not.

The paper is organized as follows. In Sec. II, we briefly review the flavor transitions of SN neutrinos as they propagate outward from deep inside a SN and traverse the Earth medium to reach the detector. We then summarize SN neutrino fluxes obtained from the simulated SN neutrino data, which will be used in our later analysis. In Sec. III, we define event rates of ν_e Ar interaction, inverse beta decay (IBD) and neutrino-proton elastic scattering (p ES) inside liquid argon and liquid scintillation detectors. These event rates are then calculated with respect to different flavor transition scenarios. In Sec. IV and V, we test the occurrence of MSW effects in SN neutrinos by comparing the time-evolution patterns of ν_e Ar event rates to those of IBD and p ES event rates with statistical uncertainties taken into account. In the case MSW effects indeed occur, we demonstrate that NMH can also be resolved by comparing the time-evolution patterns of IBD event rates to those of p ES event rates. Finally, in Sec. VI we summarize our results and conclude.

II. SUPERNOVA NEUTRINO FLUENCE

A. Primary Neutrino Flux

A SN neutrino burst lasts for $\Delta t \approx 10$ s, during which the neutronization burst happens at $t_{pb} \sim 10 - 15$ ms. Here, t_{pb} denotes the post-bounce time. In our calculation, we extract the primary neutrino fluxes from SN simulations by Nakazato *et al.* [17] for progenitor masses of 13, 20, and 30 M_\odot , and Serpico *et al.* [13] for progenitor mass of 11.2 M_\odot , accounting for SNe with iron core. The luminosity and emission curves are shown in Fig. 1, in which the Nakazato simulations (N-model) are on the left three panels and the Serpico simulation (S-model) is on the most right panel. In N-models, the neutronization burst happens at $t_{pb} \sim 10$ ms with its full width at half maximum of the luminosity $\Delta t_N \sim 30$ ms while, in S-model, the width is $\Delta t_N \sim 10$ ms. It is seen that the peak height is twice that of the tail in N-models while it is about 10 times in S-model. To encompass the whole duration of the neutronization burst, we perform our analysis for a time period of $\Delta t = 0.1$ s from the start.

These SN neutrino spectra can be well fitted by the Keil parametrization for the neutrino flux [18]

$$F_\alpha^0(E, t) = \frac{\Phi_\alpha}{\langle E_\alpha \rangle} \frac{(1 + \eta_\alpha)^{(1+\eta_\alpha)}}{\Gamma(1 + \eta_\alpha)} \left(\frac{E}{\langle E_\alpha \rangle} \right)^{\eta_\alpha} \exp \left[-(\eta_\alpha + 1) \frac{E}{\langle E_\alpha \rangle} \right], \quad (1)$$

where $\Phi_\alpha = \mathcal{L}_\alpha / \langle E_\alpha \rangle$, $\langle E_\alpha \rangle$ is the average neutrino energy, and η_α denotes the pinching

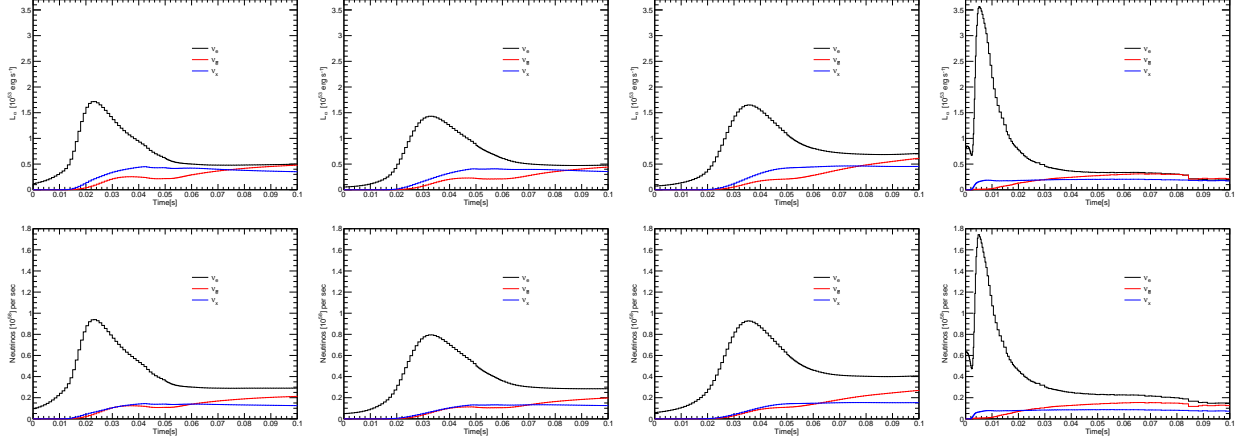


FIG. 1: Luminosities \mathcal{L}_α on the upper panel and emissions n_α on the lower panel for progenitor masses of 13, 20, 30, and $11.2 M_\odot$ from left to right, in which the first three are from the N-model and the last is from the S-model.

of the spectrum. For the period of interest, $0 \leq t \leq 0.1$ s, we summarize the relevant parameters in Table I. It can be seen that the mean energy in each neutrino component, $(\langle E_{\nu_e} \rangle, \langle E_{\bar{\nu}_e} \rangle, \langle E_{\nu_x} \rangle)$ for all the three N-models is about (10.5 MeV, 13.4 MeV, 18.7 MeV) and the mean energy for each component is (10.6 MeV, 11.9 MeV, 14.7 MeV) for the S-model. While $\langle E_{\nu_e} \rangle$ is essentially independent of the models, both $\langle E_{\bar{\nu}_e} \rangle$ and $\langle E_{\nu_x} \rangle$ for the N-model are larger than those for the S-model.

Progenitor mass [M_\odot]	13			20			30			11.2		
Flavor	ν_e	$\bar{\nu}_e$	ν_x	ν_e	$\bar{\nu}_e$	ν_x	ν_e	$\bar{\nu}_e$	ν_x	ν_e	$\bar{\nu}_e$	ν_x
$\langle E \rangle$ [MeV]	10.5	13.4	18.7	10.3	13.2	18.7	10.6	13.4	18.7	10.6	11.9	14.7
\mathcal{E} [10^{51} erg]	7.5	2.8	3.3	7.1	2.2	2.8	8.4	2.8	3.2	6.4	2.1	1.9
\mathcal{N} [10^{56}]	4.5	1.3	1.1	4.3	1.1	0.9	5.0	1.3	1.1	3.8	1.1	0.8
η	3.6	2.1	1.8	4.0	2.0	1.1	3.9	2.1	2.0	4.4	4.4	2.5

TABLE I: Keil parameters, mean energy $\langle E_\alpha \rangle$, energy emission \mathcal{E}_α , total number emitted \mathcal{N}_α (n_α integrated over time), and pinching η_α , of SN neutrino emissions for flavor α as shown in Fig. 1.

B. Neutrino Flux on Earth

In this paper, we investigate whether or not the flavor contents of SN neutrinos are modified by the MSW effect as they propagate outwards from deep inside a SN and finally reaches the Earth. In non-oscillation scenario, the flavor contents remain the same and thus the fluxes at the Earth are not changed, i.e.,

$$F_e = F_e^0, \quad F_{\bar{e}} = F_{\bar{e}}^0, \quad \text{and} \quad F_x = F_x^0. \quad (2)$$

In MSW scenarios, these fluxes shall be modified according to NMH when arriving at the detector on Earth, and can be written as:

$$F_e = F_x^0, \quad (3)$$

$$F_{\bar{e}} = (1 - \bar{P}_{2e})F_{\bar{e}}^0 + \bar{P}_{2e}F_{\bar{x}}^0, \quad (4)$$

$$4F_x = F_e^0 + F_{\bar{e}}^0 + 4F_x^0 - F_e - F_{\bar{e}} = F_e^0 + \bar{P}_{2e}F_{\bar{e}}^0 + (3 - \bar{P}_{2e})F_x^0, \quad (5)$$

for the normal hierarchy, and

$$F_e = P_{2e}F_e^0 + (1 - P_{2e})F_x^0, \quad (6)$$

$$F_{\bar{e}} = F_{\bar{x}}^0, \quad (7)$$

$$4F_x = F_e^0 + F_{\bar{e}}^0 + 4F_x^0 - F_e - F_{\bar{e}} = (1 - P_{2e})F_e^0 + F_{\bar{e}}^0 + (2 + P_{2e})F_x^0, \quad (8)$$

for the inverted hierarchy [2]. Here P_{2e} (\bar{P}_{2e}) is the probability that a mass eigenstate ν_2 ($\bar{\nu}_2$) is observed as a ν_e ($\bar{\nu}_e$) since neutrinos arrive at the Earth as mass eigenstates. We do not consider the regeneration factor due to the Earth matter effect and thus take $P_{2e} = \sin^2 \theta_{12}$. From these equations, it is shown that, in the normal hierarchy, ν_e completely comes from ν_x^0 from the source while $\bar{\nu}_e$ comes from both $\bar{\nu}_e^0$ and $\bar{\nu}_x^0$. On the other hand, in the inverted hierarchy, ν_e comes from both ν_e^0 and ν_x^0 while $\bar{\nu}_e$ completely comes from $\bar{\nu}_x^0$.

III. EVENT RATES OF SN NEUTRINOS IN TERRESTRIAL DETECTORS FOR THE NEUTRONIZATION BURST

With neutrino fluxes given above, we calculate event rates of SN neutrinos for all flavors, ν_e , $\bar{\nu}_e$, and ν_x , for the non-oscillation scenario and the case that the flavor contents are

modified by MSW effects as SN neutrinos propagate outward from the core. In the latter case, both normal and inverted hierarchies are taken into consideration. The event rates and quantities induced from these rates are displayed in numbers per bin with a 5 ms bin width throughout this article.

In liquid argon time projection chambers (LArTPC), ν_e is the most easily detected species via its charged-current interaction with argon nuclei, $\nu_e + {}^{40}\text{Ar} \rightarrow {}^{40}\text{K}^* + e^-$. The cross section for this $\nu_e\text{Ar}$ interaction has been computed in [19]. Numerical data compiled in [20] is used for our calculations. Assuming a SN at a distance of 5 kpc, the event rates of $\nu_e\text{Ar}$ in DUNE are shown in Fig. 2. It is clearly seen that time-dependence profiles of the event rates for the three N-models are highly similar while the pattern for the S-model is quite different. For the N-models, the event rates in non-oscillation scenario follow the ν_e luminosities in shape with an obvious peak followed by a much lower tail in the later half of the period. On the other hand, in MSW scenarios, those rates increase to a maximum and then decrease very slowly or remain almost unchanged. With MSW effects, the rates in the inverted hierarchy are larger than those in the normal hierarchy in the beginning and becomes smaller in the latter times. The maxima in MSW scenarios can be larger than the peak in non-oscillation scenario because ν_e and ν_x fluxes swap and, in the N-models, the ratio of $\nu_e\text{Ar}$ cross section at $\langle E_{\nu_x} \rangle \sim 18.7$ MeV to that at $\langle E_{\nu_e} \rangle \sim 10.5$ MeV is $\gtrsim 7$ while the ratio of the ν_e emission at its peak to the maximum ν_x emission is ~ 6 . For the S-model, the event rate in the non-oscillation scenario follows the luminosity curve in shape with a sharp peak followed by a long and very low tail. The event rate at the peak is about an order of magnitude larger than that of the tail. In MSW scenario, the peak event rate for the inverted hierarchy is much smaller than that of the non-oscillation scenario, and there is even no peak appearing for the normal hierarchy. This is again due to the full or partial swapping between ν_e and ν_x fluxes in MSW scenarios.

In the non-oscillation scenario, the $\nu_e\text{Ar}$ event rates at the peak for the N-models are about one half of that for the S-model since emission n_{ν_e} at the peak for the N-models are also about one half of that for the S-model, and both type of models predict approximately the same $\langle E_{\nu_e} \rangle$. On the contrary, the $\nu_e\text{Ar}$ event rates for the N-models are larger than those for the S-model in MSW scenarios at later times. To account for this, we note that both n_{ν_x} and $\langle E_{\nu_x} \rangle$ in the N-models are larger than those in the S-model. Since $\nu_e\text{Ar}$ cross section increases rapidly with the neutrino energy, the full or partial swapping between ν_e

and ν_x fluxes in MSW scenarios hence favors the ν_e Ar event rates in N-models.

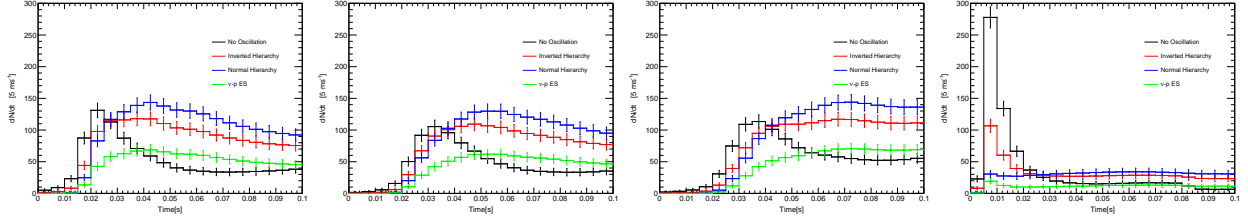


FIG. 2: Event rates of ν_e Ar in DUNE in different flavor transition scenarios with event rates of p ES in JUNO as a reference. These event rates are obtained with progenitor masses of 13, 20, and 30 M_\odot in the N-model and 11.2 M_\odot in the S-model, from left to right.

In scintillation detectors, the spectrum of inverse beta decay (IBD) events is established by measuring the positron energy deposit. The observed event spectrum and total number of IBD events are given by

$$\left(\frac{dN}{dE_{e^+}} \right) = N_p \cdot \int dE_\nu \frac{dF_{\bar{e}}}{dE_\nu} \cdot \frac{d\sigma_{\text{IBD}}(E_\nu, E_{e^+})}{dE_{e^+}}, \quad (9)$$

$$N_{\text{IBD}} = N_{e^+} = N_p \cdot \int_{E_{\min}}^{\infty} dE_\nu \frac{dF_{\bar{e}}}{dE_\nu} \cdot \sigma_{\text{IBD}}(E_\nu), \quad (10)$$

where N_p is the number of target protons in the detector and the IBD cross section $\sigma_{\text{IBD}}(E_\nu)$ is taken from [21]. The minimum neutrino energy for generating IBD interaction is $E_{\min} = 1.8$ MeV. The IBD event rates in JUNO [22] are shown in Fig. 3.

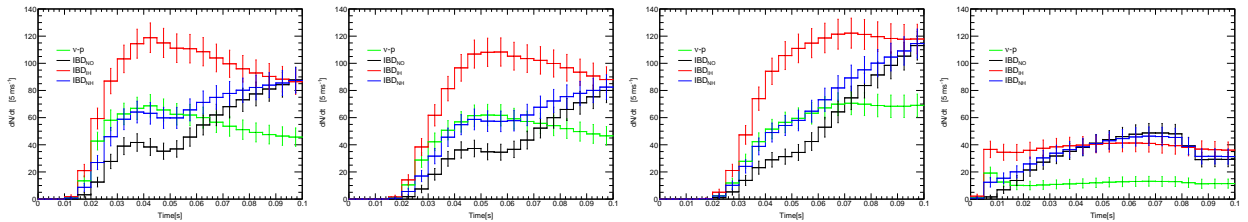


FIG. 3: IBD event rates for different flavor scenarios with p ES event rates as a reference.

These event rates are obtained with progenitor masses of 13, 20, and 30 M_\odot in the N-model and 11.2 M_\odot in the S-model, from left to right.

IBD event rates accounts for $\bar{\nu}_e$ fluxes. In N-models, $n_{\bar{\nu}_e}$ is comparable to n_{ν_x} in the earlier time as seen in Fig. 1. MSW oscillation does not change the situation since it involves only the full swapping (inverted hierarchy) or partial swapping (normal hierarchy) between $\bar{\nu}_e$ and ν_x . On the other hand, the mean energies of ν_x is larger than that of $\bar{\nu}_e$ as described in

Table I. Since IBD cross section grows with the neutrino energy, the full and partial swaps between $\bar{\nu}_e$ and ν_x in Eqs. (4) and (7) indicate that IBD event rate for the inverted hierarchy in MSW scenario is larger than that for the normal hierarchy, which in turn is larger than the IBD event rate in the non-oscillation scenario. In the later time, $n_{\bar{\nu}_e}$ becomes larger than n_{ν_x} , hence IBD event rates for different scenarios gradually converge.

For the S-model, the IBD event rate for the inverted hierarchy follows the luminosity and emission curves of ν_x flux with a sudden rise in the beginning followed by a plateau since ν_e and ν_x fully swap as indicated in Eq. (7). For the normal hierarchy, the IBD event rates is comparable to that of non-oscillation scenario, which resembles the luminosity and emission curves of the ν_x flux.

Inside the liquid scintillation detector, the neutrino-proton elastic scatterings (p ES) can contribute a comparable number of events to that of IBD due to the large number of free protons [23]. The observed event spectrum is given as

$$\frac{dN}{dT'} = \frac{N_p}{dT'/dT} \int_{E_{\nu,\min}}^{\infty} dE_{\nu} \frac{dF_{\text{tot}}}{dE_{\nu}} \frac{d\sigma_{\nu p}(E_{\nu}, T)}{dT}, \quad (11)$$

where $F_{\text{tot}} \equiv F_e + F_{\bar{e}} + 4F_x$ is the total fluence of SN neutrinos and T is the recoil kinetic energy of protons which are scattered by SN neutrinos. To produce a proton recoil energy T requires a minimum neutrino energy $E_{\nu,\min} = \sqrt{m_p T/2}$, with m_p the proton mass. In other words, a neutrino of energy E_{ν} can produce a proton recoil energy between 0 and $T_{\max} = 2E_{\nu}^2/m_p$. These protons are slow hence they are detected with quenched energies $T' < T$. The proton recoil energy T is mapped to an electron-equivalent quenched energy T' through the quenching function

$$T'(T) = \int_0^T \frac{dT}{1 + k_B \langle dT/dx \rangle + C \langle dT/dx \rangle^2}, \quad (12)$$

where $k_B = 0.00759$, Birks constant [24], and $C = 2.05 \times 10^{-6}$ are taken from [22] for JUNO detector. The number of p ES events is then given by

$$N_{p\text{ES}} = N_p \cdot \int_{T_{\min}}^{\infty} \int_{E_{\nu,\min}}^{\infty} \frac{dF_{\text{tot}}}{dE_{\nu}} \cdot \frac{d\sigma_{\nu p}(E_{\nu}, T)}{dT} dE_{\nu} dT, \quad (13)$$

where the differential cross section, $d\sigma_{\nu p}/dT$, is taken from [23, 25]. We point out that not all signals within the energy range of proton recoils are not detectable. Since the scintillator is made of hydrocarbon, a natural isotope of the carbon, ^{14}C , decays into ^{14}N , emitting electrons below 0.2 MeV with a high rate. Below this energy, the signal is flooded by very

low energy electrons. Therefore, a threshold of $T'_{\min} = 0.2$ MeV is set for recording the signal. The threshold of $T'_{\min} = 0.2$ MeV is converted to the threshold of proton recoil energy T_{\min} , e.g. $T_{\min} = 0.93$ MeV for JUNO detector. We show the p ES event rates as a reference in both Figs. 2 and 3 since p ES interactions are flavor blind and account for the total neutrino flux.

Progenitor mass [M_{\odot}]	13			20			30			11.2		
Signal	ν_e Ar	IBD	p ES	ν_e Ar	IBD	p ES	ν_e Ar	IBD	p ES	ν_e Ar	IBD	p ES
Non-oscillation	1047	967	934	956	776	822	1189	994	915	848	639	238
MSW-NH	1982	1194	934	1750	997	822	1922	1199	915	612	672	238
MSW-IH	1697	1703	934	1507	1492	822	1697	1661	915	685	747	238

TABLE II: Total numbers of SN neutrino events for ν_e Ar, IBD, and p ES signals in different flavor transition scenarios within the period of interest.

Table II presents total event numbers of the calculated event rates shown in Figs. 2 and 3. For the S-model, the total event number of each signal is smaller than that for the N-model in all corresponding scenarios. This corresponds to the fact that, for each of the neutrino flavor, the total energy release and particle emission for the S-model are smaller than those for the N-model. It is seen that IBD event numbers in MSW scenarios are larger than those in the non-oscillation scenario for both N- and S-models. This results from the fact that the increase in IBD cross section overwhelms the decrease in the neutrino emission when $\bar{\nu}_e$ and ν_x swap with each other. For the N-model, the IBD cross section at $\langle E_{\nu_x} \rangle \sim 18.7$ MeV is about twice of that at $\langle E_{\bar{\nu}_e} \rangle \sim 13.4$ MeV while the total emission of ν_x is $\sim 85\%$ of that of $\bar{\nu}_e$. For the S-model, the IBD cross section at $\langle E_{\nu_x} \rangle \sim 14.7$ MeV is ~ 1.5 times of that at $\langle E_{\bar{\nu}_e} \rangle \sim 11.9$ MeV while the total emission of ν_x is $\sim 73\%$ of that of $\bar{\nu}_e$.

Concerning ν_e Ar detection mode, the event numbers in MSW scenarios are larger than those in the non-oscillation scenario for N-models. For S-model, the event numbers in MSW scenarios are smaller than their counterpart in the non-oscillation scenario. In the N-model, ν_e Ar cross section at $\langle E_{\nu_x} \rangle \sim 18.7$ MeV is $\gtrsim 7$ times of that at $\langle E_{\nu_e} \rangle \sim 10.5$ MeV and the total emission of ν_x is $\gtrsim 1/5$ times of that of ν_e . Similar to the case of IBD events, the increase in ν_e Ar cross section overwhelms the decrease in neutrino emission so that the

number of ν_e Ar events increases when ν_e flux swaps with ν_x flux due to MSW effects. In the S-model, ν_e Ar cross section at $\langle E_{\nu_x} \rangle \sim 14.7$ MeV is $\lesssim 4$ times of that at $\langle E_{\nu_e} \rangle \sim 10.6$ MeV and the total emission of ν_x is $< 1/4$ times of that of ν_e . Contrary to the case of N-models, the increase in ν_e Ar cross section cannot make up the decrease in neutrino emission in the S-model so that the number of ν_e Ar events decreases when ν_e flux swaps with ν_x flux due to MSW effects.

Besides these signals of interests, SN neutrinos also interact in the following channels: (1) the elastic neutrino-electron scattering $\nu + e^- \rightarrow \nu + e^-$, (2) the charged-current ν_e interaction $\nu_e + {}^{12}\text{C} \rightarrow {}^{12}\text{N}_{\text{g.s.}} + e^-$, (3) the charged-current $\bar{\nu}_e$ interaction $\bar{\nu}_e + {}^{12}\text{C} \rightarrow {}^{12}\text{B}_{\text{g.s.}} + e^+$, (4) proton knockouts [27] $\nu(\bar{\nu}) + {}^{12}\text{C} \rightarrow {}^{11}\text{B} + p + \nu(\bar{\nu})$ and $\nu + {}^{12}\text{C} \rightarrow {}^{11}\text{C} + e^- + p$, and (5) the 15.11 MeV de-excitation line $\nu(\bar{\nu}) + {}^{12}\text{C} \rightarrow \nu(\bar{\nu}) + {}^{12}\text{C}^*$ in scintillation detectors and, in LAr TPC detectors, (6) $\nu + e^- \rightarrow \nu + e^-$ and (7) $\bar{\nu}_e$ Ar charged-current interaction, $\bar{\nu}_e + {}^{40}\text{Ar} \rightarrow {}^{40}\text{Cl}^* + e^+$. The event rates of the above channels are subdominant compared to ν_e Ar, IBD, and p ES channels (for a reference, see Table II in [27] and Table I in [28]). Therefore, we neglect their contributions and focus on ν_e Ar, IBD, and p ES interactions.

IV. TESTING THE OCCURRENCE OF MSW EFFECTS

To account for the sharp rise of ν_e flux during the neutronization burst, we define cumulative time distributions of the SN neutrino signals for the time interval of interest $t = 0 - 0.1\text{s}$ as in [13]

$$K(t) = \frac{\int_0^t \frac{dN}{dt} dt}{\int_0^{0.1\text{s}} \frac{dN}{dt} dt}. \quad (14)$$

In Fig. 4, we present K_{Ar} and K_{IBD} , the cumulative distributions of ν_e Ar and IBD event rates on the upper and lower panels, respectively, in non-oscillation scenario and NH and IH MSW scenarios. By definition, $0 \leq K(t) \leq 1$. It is clearly seen that, on the upper panel, the cumulative ν_e Ar signals exhibit convexity in the non-oscillation scenario while, with MSW effects, the cumulative distributions are approximately linear in both mass hierarchies. For the S-model, the cumulative distribution K_{Ar} is more convex since the time profile of ν_e Ar event rate is sharper with larger fraction of events occurring in the peak region. On the lower panel, the cumulative distribution K_{IBD} exhibits concavity in the non-oscillation scenario while, with MSW effects, the cumulative distributions are approximately linear in both

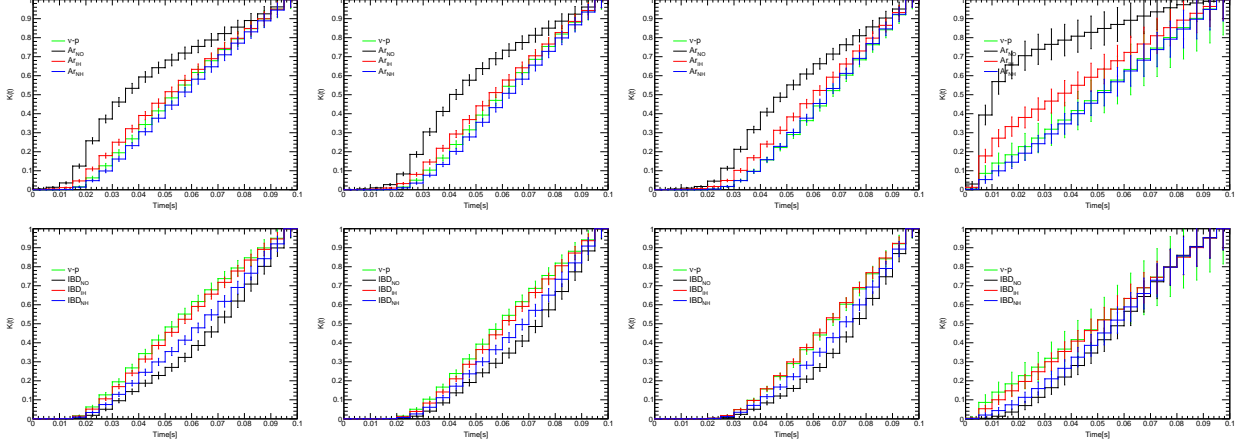


FIG. 4: Cumulative distribution of $\nu_e \text{Ar}$ signals on the upper panel, and of IBD signals on the lower panel, in the time period of $0 \leq t \leq 0.1$ s. The left three columns in each panel are predictions of N-model for progenitor masses of 13, 20, and 30 M_\odot , from left to right. The most right column in each panel is the prediction of S-model for a progenitor mass of 11.2 M_\odot .

mass hierarchies. To clearly distinguish the non-oscillation scenario from MSW oscillations, a ratio between the cumulative distributions, K_{Ar} and K_{IBD} , is defined as

$$R_{\text{cum}}(t) \equiv \frac{2}{3} \left(\frac{1 + K_{\text{Ar}}(t)}{1 + K_{\text{IBD}}(t)} \right) - \frac{1}{3}. \quad (15)$$

From $K_{\text{Ar}}(0) = K_{\text{IBD}}(0) = 0$ and $K_{\text{Ar}}(0.1 \text{ s}) = K_{\text{IBD}}(0.1 \text{ s}) = 1$, one has $R_{\text{cum}}(0) = R_{\text{cum}}(0.1 \text{ s}) = 1/3$. We point out that K_{Ar} in the non-oscillation case is larger than those in MSW scenarios while K_{IBD} behaves in an opposite way. Hence it is clear that R_{cum} in the non-oscillation case is larger than those in MSW scenarios. The maximum of R_{cum} in the non-oscillation case is also expected to be much larger than those in MSW scenarios. Therefore R_{cum} is a good discriminator to distinguish the non-oscillation scenario from MSW oscillations. As shown in Fig. 5, R_{cum} in the non-oscillation scenario exhibits a large bulge while, in MSW scenarios, only small bumps emerge in the time evolution of R_{cum} . In the non-oscillation case, the maximum of R_{cum} is ~ 0.55 for the N-model and ~ 0.75 for the S-model while, in MSW scenarios, the maximum is ~ 0.38 for the N-model and ~ 0.45 for the S-model. One can see that black curves for R_{cum} in the non-oscillation scenarios and colored curves for R_{cum} in MSW scenarios are clearly discriminated. In other words, the behaviors of R_{cum} determine whether or not MSW effects occur in the propagation of SN neutrinos.

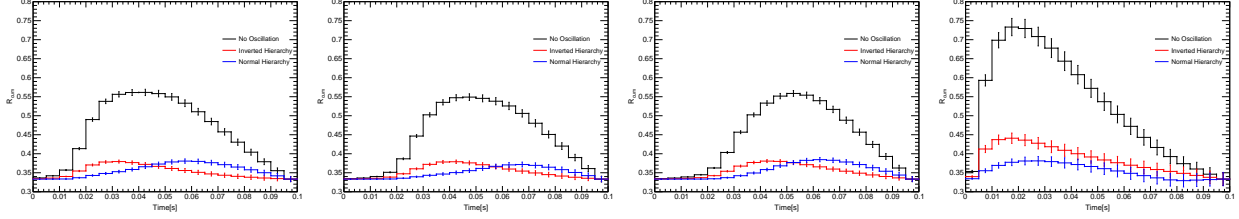


FIG. 5: R_{cum} in the time period of $0 \leq t \leq 0.1$ s. The left three columns in each panel are predictions of N-model for progenitor masses of 13, 20, and 30 M_{\odot} , from left to right. The most right column in each panel is the prediction of S-model for a progenitor mass of 11.2 M_{\odot} .

V. RESOLVING NEUTRINO MASS HIERARCHY

While the comparison between $\nu_e\text{Ar}$ and IBD event rates can probe the occurrence of MSW effects independent of the NMH, the inclusion of $p\text{ES}$ event rates can help to further distinguish between normal and inverted hierarchies. Before comparing $\nu_e\text{Ar}$ and IBD event rates to $p\text{ES}$ ones, these event rates are normalized to their corresponding total events within the period of $0 \leq t \leq 0.1$ s. The normalized $\nu_e\text{Ar}$ and IBD event rates are shown on the upper and lower panels in Fig. 6, respectively, with $p\text{ES}$ ones as a reference.

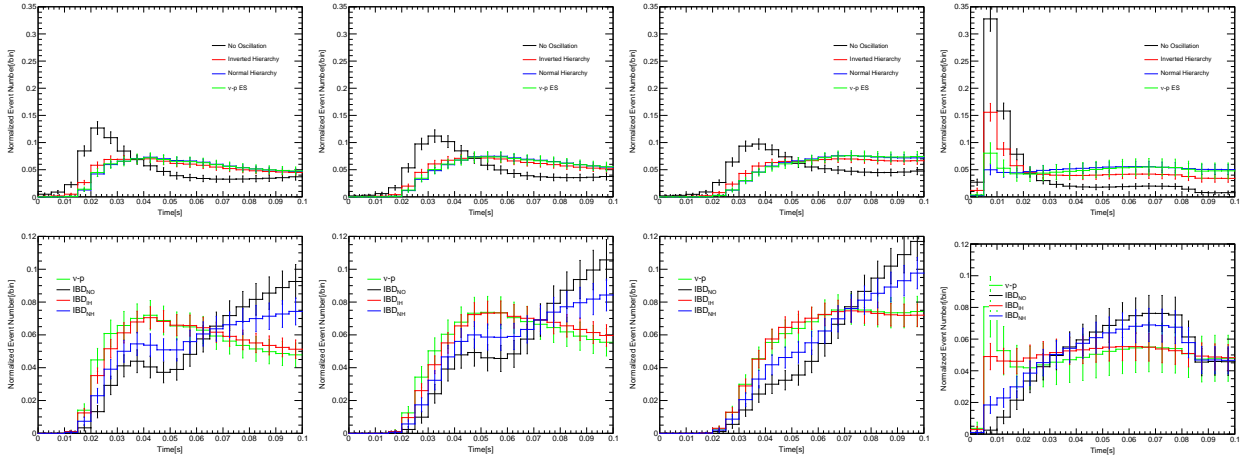


FIG. 6: Normalized $\nu_e\text{Ar}$ and IBD event rates on the upper and lower panels, respectively, with normalized $p\text{ES}$ event rates as a reference in the time period of $0 \leq t \leq 0.1$ s. The left three columns in each panel are predictions of N-model for progenitor masses of 13, 20, and 30 M_{\odot} , from left to right. The most right column in each panel is the prediction of S-model.

The shape of each normalized event rate should in principle follow its corresponding event rate in Figs. 2 and 3 for ν_e Ar and IBD event rates, respectively. Since the curves in Fig. 6 are obtained by normalizing to different event numbers, their slopes are modified accordingly. Analogous to defining the cumulative ratio of ν_e Ar to IBD in Eq.(15), we define the following modified ratios for normalized event rates:

$$R_{\text{Ar,pES}}(t) \equiv \frac{2}{3} \left(\frac{1 + N_{\text{Ar}}(t)}{1 + N_{\text{pES}}(t)} \right) - \frac{1}{3}, \text{ and } R_{\text{IBD,pES}}(t) \equiv \frac{2}{3} \left(\frac{1 + N_{\text{IBD}}(t)}{1 + N_{\text{pES}}(t)} \right) - \frac{1}{3}, \quad (16)$$

where $N_{\text{Ar}}(t)$, $N_{\text{IBD}}(t)$, and $N_{\text{pES}}(t)$ are normalized event rates shown in Fig. 6. In Fig. 7, we show $R_{\text{Ar,pES}}(t)$ and $R_{\text{IBD,pES}}(t)$ on upper and lower panels, respectively. Those plots in the left three columns of each panel are predictions of N-model while plots in the most right column are predictions of S-model.

For N-model, $R_{\text{Ar,pES}}(t)$ goes to a maximum larger than 0.37 and decreases to a minimum about 0.31, exhibiting large fluctuation in the non-oscillation scenario while it varies much smoothly between 0.34 and 0.33 for both mass hierarchies in MSW scenarios. Therefore, the pattern of $R_{\text{Ar,pES}}(t)$ can be used to determine the occurrence of MSW effects, provided N-model is applicable to describe the SN neutrino flux. On the lower panel, $R_{\text{IBD,pES}}(t)$ is almost stationary in the MSW scenario of inverted hierarchy while it increases from a trough with a significant slope of $\gtrsim 0.6 \text{ s}^{-1}$ during the later half of the period for the normal hierarchy in the MSW scenario and in the non-oscillation scenario. In the case that MSW effects is confirmed by $R_{\text{cum}}(t)$ and/or $R_{\text{Ar,pES}}(t)$, one can use $R_{\text{IBD,pES}}(t)$ to determine the NMH.

However, the situation is different when we turn to the results given by the S-model, which are shown in the most right column of plots in Fig. 7. In the non-oscillation scenario, $R_{\text{Ar,pES}}(t)$ also exhibits a large fluctuation with an even higher maximum of $\gtrsim 0.5$ and a long tail gradually decreasing to 0.31. In MSW scenarios, $R_{\text{Ar,pES}}(t)$ shows a clear peak for the inverted hierarchy and a dip for the normal hierarchy despite the smooth tails. Clearly, it is not sufficient to determine whether MSW effects occur or not with only the pattern of $R_{\text{Ar,pES}}(t)$ for the S-model. On the lower panel, uncertainties $R_{\text{IBD,pES}}(t)$ are such large that all three curves can not be distinguished from one another. Even though MSW effects in SN neutrinos can be confirmed with $R_{\text{Ar,pES}}(t)$, neutrino hierarchy still cannot be determined in the S-model as opposed to the N-model case.

When the predictions of both N- and S-model are taken for considerations, MSW scenario

for the inverted hierarchy in the S-model cannot be clearly distinguished from the non-oscillation scenario in the N-model, since peak heights of $R_{\text{Ar,pES}}(t)$ in both cases are nearly identical, ~ 0.38 . Because the current understanding of SN explosions is not sufficient to discriminate between N- and S-model, one cannot conclude whether MSW effects occur or not with time profiles of $R_{\text{Ar,pES}}(t)$.

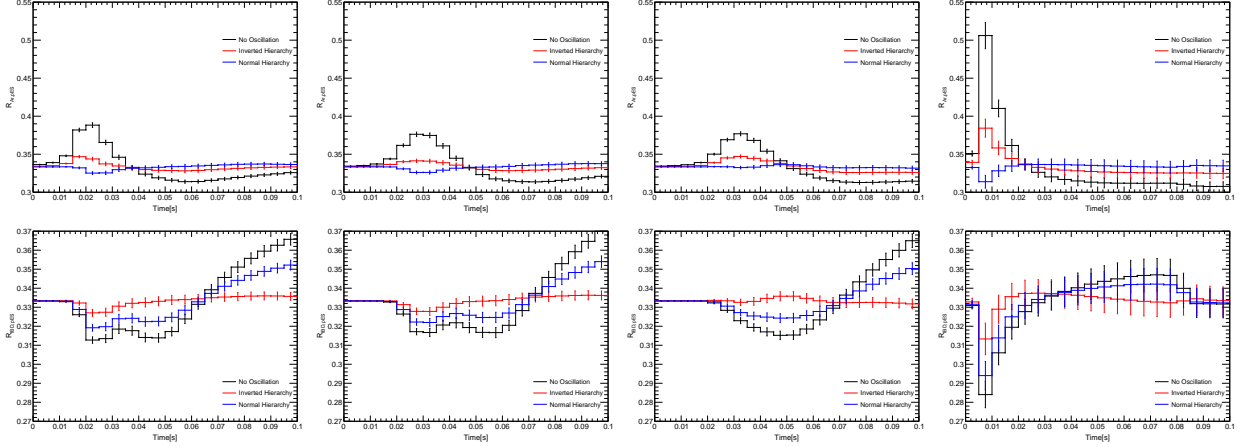


FIG. 7: Time profiles of $R_{\text{Ar,pES}}(t)$ (upper panel) and $R_{\text{IBD,pES}}(t)$ (lower panels) for $0 \leq t \leq 0.1$ s. The left three columns in each panel are predictions of N-model for progenitor masses of 13, 20, and 30 M_{\odot} , from left to right. The most right column in each panel is the prediction of S-model.

VI. SUMMARY AND CONCLUSIONS

We have proposed to verify MSW effects in SN neutrinos and identify the neutrino mass hierarchy by using the time evolution of SN neutrino event rates during the neutronization burst. These event rates are calculated with SN neutrino emissions extracted from SN simulation data by two different groups, denoted as the N- and S-models [13, 17]. The differences of neutrino emissions between the two models are analyzed. To cover the mass range of the iron-core SNe, we perform our analysis with data from progenitor masses of 13, 20, and 30 M_{\odot} in the N-model.

With event rates of $\nu_e\text{Ar}$ in liquid argon detectors and those of IBD and $p\text{ES}$ in scintillation detectors, we define a cumulative event ratio R_{cum} in Eq. (15) and modified event ratios $R_{\text{Ar,pES}}(t)$ and $R_{\text{IBD,pES}}(t)$ in Eq. (16). We then demonstrate that, for both the N- and S-models, time-evolution patterns of R_{cum} are effective in determining whether MSW effects

occur or not. However, the subsequent analysis on $R_{\text{Ar,pES}}(t)$ and $R_{\text{IBD,pES}}(t)$ renders model-dependent results. For the N-model, we show that $R_{\text{Ar,pES}}(t)$ is also useful in determining the occurrence of MSW effects. In the case that MSW effect in SN neutrinos is favored in this model, we show that the time-evolution patterns of the modified ratio $R_{\text{IBD,pES}}(t)$ can be used to identify the neutrino mass hierarchy. For the S-model, we show that $R_{\text{Ar,pES}}(t)$ is not decisive in determining the occurrence of MSW effects. We also find that the uncertainties in $R_{\text{IBD,pES}}(t)$ are so large that the three flavor transition scenarios for SN neutrinos cannot be distinguished from one another.

It is seen that the cumulative ratio $R_{\text{cum}}(t)$ is capable of determining the occurrence of MSW effects in SN neutrinos for both N- and S-models. The basis of our method is the unique pattern of the primary ν_e emission, which is different from the shapes of $\bar{\nu}_e$ and ν_x emissions. MSW oscillations moderate the sharp peak of ν_e Ar event rates in the N-model while the peak is maintained for the inverted hierarchy in the S-model as seen in Fig. 2. However, we note that the time profiles of IBD event rates in both models are modified significantly by MSW oscillation for the inverted hierarchy as seen in Fig. 3. Hence $R_{\text{cum}}(t)$ constructed from ν_e Ar and IBD events rates is a good test to MSW oscillations in SN neutrinos.

The ratio variables we use are derived from event rates of ν_e Ar, IBD, and pES in terrestrial detectors and these event rates are calculated with SN neutrino emissions extracted from SN simulation data. We perform our analysis with simulation data of progenitor masses of 13, 20, 30, and 11.2 M_\odot from two different groups. Our work not only covers the mass range of the core-collapse SNe with iron-core but also takes different possibilities in simulation of SN neutrino emissions. Although SN neutrino emission for each flavor depends on the progenitor model, the time evolutions of the neutrino emissions and their luminosity curves exhibit common behaviors, based on which is our method to determine whether MSW effects occur or not. Hence, our method can be applied to all core-collapse SNe with iron-cores.

Acknowledgements

The work is by the Ministry of Science and Technology, Taiwan under Grant No. 107-2119-M-009-017-MY3.

- [1] A. Mirizzi, I. Tamborra, H. T. Janka, N. Saviano, K. Scholberg, R. Bollig, L. Hudepohl and S. Chakraborty, Riv. Nuovo Cim. **39** (2016) no.1-2, 1, arXiv:1508.00785
- [2] A. S. Dighe and A. Y. Smirnov, Phys. Rev. D **62**, 033007 (2000), arXiv:hep-ph/9907423.
- [3] H. Duan, G. M. Fuller, J. Carlson and Y. Z. Qian, Phys. Rev. D **74** (2006) 105014, astro-ph/0606616.
- [4] S. Hannestad, G. G. Raffelt, G. Sigl and Y. Y. Y. Wong, Phys. Rev. D **74**, 105010 (2006), Phys. Rev. D **76**, 029901 (2007), astro-ph/0608695.
- [5] H. Duan, G. M. Fuller and Y. Z. Qian, Ann. Rev. Nucl. Part. Sci. **60**, 569 (2010), arXiv:1001.2799.
- [6] R. F. Sawyer, Phys. Rev. D **72** (2005) 045003, hep-ph/0503013.
- [7] R. F. Sawyer, Phys. Rev. D **79** (2009) 105003, arXiv:0803.4319.
- [8] R. F. Sawyer, Phys. Rev. Lett. **116** (2016) no.8, 081101, arXiv:1509.03323.
- [9] S. Chakraborty, R. S. Hansen, I. Izaguirre and G. Raffelt, JCAP **1603** (2016) 042, arXiv:1602.00698.
- [10] C. Lunardini and A. Yu Smirnov, J. Cosm. Astropart. Phys. **06**, 009 (2003), arXiv:hep-ph/0302033.
- [11] B. Dasgupta, A. Dighe, A. Mirizzi, Phys. Rev. Lett. **101** 171801 (2008), arXiv:08021481.
- [12] H. Duan, G. M. Fuller, J. Carlson, Y. Z. Qian, Phys. Rev. Lett. **99**, 241802 (2007), arXiv:0707.0290.
- [13] P. D. Serpico, S. Chakraborty, T. Fischer, L. Hudepohl, H. T. Janka and A. Mirizzi, Phys. Rev. D **85** (2012) 085031, arXiv:1111.4483.
- [14] S. H. Chiu, C.-C. Huang, and K.-C. Lai, PTEP 2015 6, 063B01(2015), arXiv:1312.4262.
- [15] K.-C. Lai, F.-F. Lee, F.-S. Lee, G.-L. Lin, T.-C. Liu and Y. Yang, JCAP **1607**, no. 07, 039 (2016), arXiv:1603.00692.
- [16] D. Vale, T. Rauscher and N. Paar, JCAP **1602** (2016) 007, arXiv:1509.07342.

- [17] K. Nakazato, K. Sumiyoshi, H. Suzuki, T. Totani, H. Umeda and S. Yamada, *Astrophys. J. Suppl.* **205** (2013) 2, arXiv:1210.6841.
- [18] M. T. Keil, G. G. Raffelt, and H.-T. Janka, *Astrophys. J.* **590**, 971 (2003), arXiv:astro-ph/0208035.
- [19] E. Kolbe, K. Langanke, G. Martinez-Pinedo and P. Vogel, *J. Phys. G* **29** (2003) 2569, nucl-th/0311022.
- [20] K. Scholberg, *Ann. Rev. Nucl. Part. Sci.* **62** (2012) 81, arXiv:1205.6003.
- [21] A. Strumia and F. Vissani, *Phys. Lett. B* **564** (2003) 42, astro-ph/0302055.
- [22] F. An *et al.* [JUNO Collaboration], *J. Phys. G* **43**, no. 3, 030401 (2016), arXiv:1507.05613.
- [23] B. Dasgupta and J. F. Beacom, *Phys. Rev. D* **83**, 113006(2011), arXiv:hep-ph/1103.2768.
- [24] J.B. Birks, *Proc. Phys. Soc. Lond. Sect. A* **64**, 874 (1951).
- [25] J. F. Beacom, W. M. Farr and P. Vogel, *Phys. Rev. D* **66**, 033001 (2002), arXiv:0205220.
- [26] G. Alimonti *et al.* [Borexino Collaboration], *Astropart. Phys.* **16**, 205 (2002).
- [27] C. Lujan-Peschard, G. Pagliaroli and F. Vissani, *JCAP* **1407**, 051 (2014), arXiv:1402.6953.
- [28] Jia-Shu Lu, Yu-Feng Li and Shun Zhou, *Phys. Rev. D* **94**, 023006 (2016), arXiv:1605.07803.